

# S-Shaped Suppression of the Superconducting Transition Temperature in Cu-Intercalated NbSe<sub>2</sub>

Huixia Luo,<sup>†,‡</sup> Judyta Strychalska-Nowak,<sup>§</sup> Jun Li,<sup>||</sup> Jing Tao,<sup>||</sup> Tomasz Klimczuk,<sup>§</sup> and Robert J. Cava<sup>†</sup>

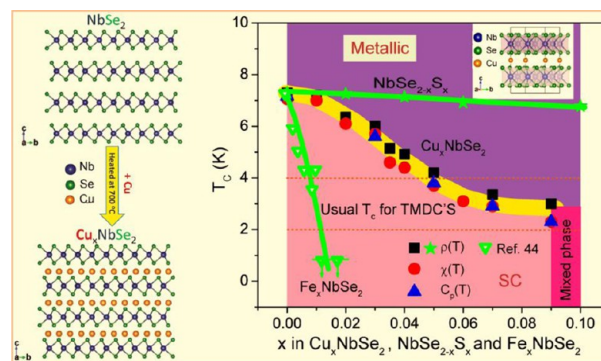
<sup>†</sup>Department of Chemistry, Princeton University, Princeton, New Jersey 08544, United States

<sup>‡</sup>School of Materials Science and Engineering, Sun Yat-Sen University, No. 135, Xingang Xi Road, Guangzhou 510275, P. R. China

<sup>§</sup>Faculty of Applied Physics and Mathematics, Gdansk University of Technology, Narutowicza 11/12, 80-233 Gdansk, Poland

<sup>||</sup>Condensed Matter Physics and Materials Science Departments, Brookhaven National Laboratory, Upton, New York 11973, United States

**ABSTRACT:** 2H-NbSe<sub>2</sub> is the prototype and most frequently studied of the well-known transition metal dichalcogenide (TMDC) superconductors. As 2H-NbSe<sub>2</sub> is widely acknowledged as a conventional superconductor, its transition temperature to the superconducting state ( $T_c$ ) is 7.3 K, a  $T_c$  that is substantially higher than those seen for the majority of TMDCs, where  $T_c$  values between 2 and 4 K are the norm. Here we report the intercalation of Cu into 2H-NbSe<sub>2</sub> to make Cu<sub>x</sub>NbSe<sub>2</sub>. As is typically found when chemically altering an optimal superconductor,  $T_c$  decreases with an increase in  $x$ , but the way that  $T_c$  is suppressed in this case is unusual: an S-shaped character is observed, with an inflection point near  $x = 0.03$  and, at higher  $x$  values, a leveling off of the  $T_c$  near 3 K, down to the usual value for a layered TMDC. Electronic characterization reveals corresponding S-like behavior for many of the parameters of the materials that influence  $T_c$ . To illustrate its character, the superconducting phase diagram for Cu<sub>x</sub>NbSe<sub>2</sub> is contrasted with those of Fe<sub>x</sub>NbSe<sub>2</sub> and NbSe<sub>2-x</sub>S<sub>x</sub>.



## ■ INTRODUCTION

Transition metal dichalcogenides (TMDCs) have been studied for decades because of the rich electronic properties that arise because of their low structural dimensionality. These systems share the MX<sub>2</sub> formula, where M is a transition metal (M = Ti, Zr, Hf, V, Nb, Ta, Mo, W, or Re) and X is a chalcogen (X = S, Se, or Te);<sup>1-4</sup> the structures are made from stacking X-M-X layers in repeating patterns, with van der Waals (VdW) bonding between the layers. 2H-NbSe<sub>2</sub> was one of the earliest layered TMDC materials known to superconduct, with a critical temperature ( $T_c$ ) of ~7.3 K. This  $T_c$  is significantly higher than those encountered for the many other known TMDC superconductors, for which  $T_c$  is commonly in the range of 2–4 K. 2H-NbSe<sub>2</sub> also hosts a quasi-two-dimensional incommensurate charge density wave (ICDW) with a  $T_{CDW}$  of ~33 K.<sup>5</sup> It is the most studied of the layered transition metal dichalcogenide superconductors, with almost countless experimental and theoretical papers focusing on its behavior over the past 50 years (see, e.g., refs 6–14). The relation between Fermi surface nesting and its superconductivity is still under debate,<sup>12</sup> for example, even though 2H-NbSe<sub>2</sub> has been considered a conventional superconductor for decades.<sup>13</sup> In addition, because of new, recently developed concepts, such as d-wave pairing in cuprates<sup>14</sup> and two-gap superconductivity in MgB<sub>2</sub>,<sup>15-17</sup> there have been more studies of the super-

conducting order parameters of 2H-NbSe<sub>2</sub>.<sup>18-21</sup> Many recent experiments performed on 2H-NbSe<sub>2</sub>, including specific heat,<sup>18</sup> thermal conductivity,<sup>19</sup> magnetization,<sup>20</sup> penetration depth,<sup>21</sup> tunneling spectroscopy,<sup>22-24</sup> and angle-resolved photoemission spectroscopy (ARPES) experiments,<sup>25-29</sup> agree that more than one energy scale is important for superconductivity. Evidence of strong gap anisotropy in 2H-NbSe<sub>2</sub> thus appears to be well established, but the question of whether this is a result of there being different superconducting gaps on different Fermi surface sheets or whether it originates elsewhere remains under discussion.

Here we report the results of the intercalation of Cu into 2H-NbSe<sub>2</sub> to form Cu<sub>x</sub>NbSe<sub>2</sub><sup>30</sup> in the doping range of  $0 \leq x \leq 0.09$ , where the 2H structure (see Figure 1A) is maintained; above  $x = 0.09$ , the material is multiphase and deductions about  $T_c$  cannot reliably be made. The  $T_c$  decreases with an increasing Cu content in Cu<sub>x</sub>NbSe<sub>2</sub>, as is commonly found upon introduction of “impurities” into optimal superconductors, but the way that superconductivity is suppressed is unusual. An S-shaped character is observed in  $T_c$  versus  $x$ , with an inflection point near  $x = 0.03$  and a leveling off, at higher values of  $x$ , of

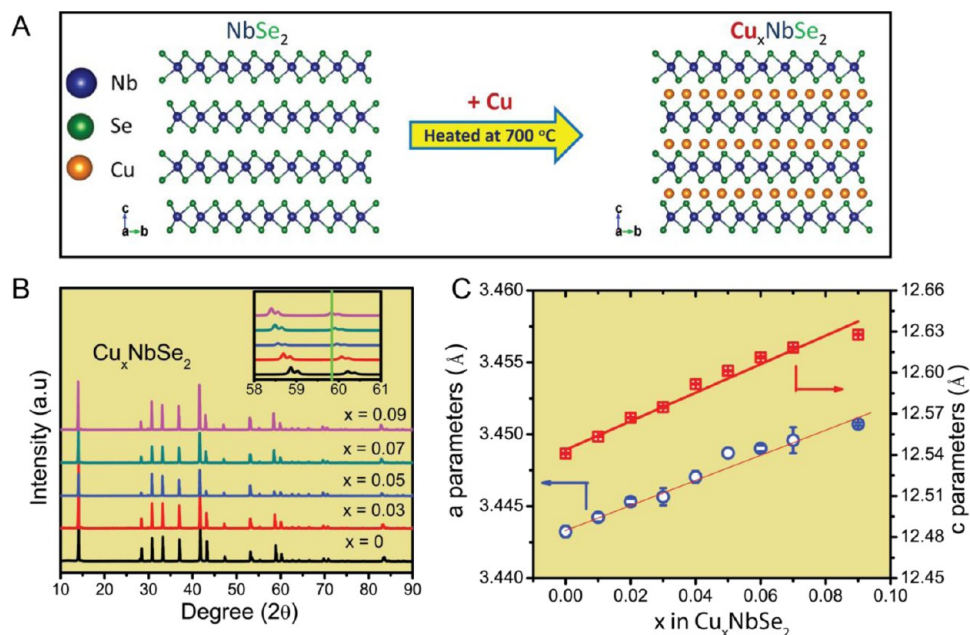


**Figure 1.** Structural and chemical characterization of  $\text{Cu}_x\text{NbSe}_2$ . (A) Flowchart for Cu intercalation of 2H-NbSe<sub>2</sub>. The copper-doped materials are synthesized directly from the elements. (B) Powder XRD patterns (Cu  $K\alpha$ ) for the  $\text{Cu}_x\text{NbSe}_2$  samples studied ( $0 \leq x \leq 0.09$ ). The inset shows a detail of the diffracted angle region where the effect of the increasing cell parameters with an increasing level of Cu intercalation can clearly be seen. (C) Composition dependence of the room-temperature lattice parameters for  $\text{Cu}_x\text{NbSe}_2$  ( $0 \leq x \leq 0.09$ ); standard deviations are shown when they are larger than the plotted points.

the abnormally high 7 K  $T_c$  in the pure phase to a  $T_c$  value near 3 K, back down to where it is commonly observed for a layered TMDC. The materials are characterized through measurements of their resistivities, critical fields, magnetic susceptibilities, and heat capacities, which reveal a corresponding S-shaped behavior in the electronic properties of the system, most notably the electronic contribution to the specific heat and the electron-phonon coupling parameter. CDWs compete with superconductivity for stability at low temperatures in the layered TMDCs, and thus the effect of Cu intercalation on the CDW is of interest for obtaining a fuller picture of the electronic system. Our temperature-dependent electron diffraction study reveals a minor change in the  $\mathbf{q}$  vector of the CDW upon Cu intercalation, degradation but not destruction of the coherence of the CDW, especially in the direction perpendicular to the layers, and also the extension of CDW fluctuations, evidenced by diffuse scattering, to room temperature. Comparison of the superconducting phase diagram for  $\text{Cu}_x\text{NbSe}_2$  to those for the other doped 2H-NbSe<sub>2</sub> materials,  $\text{Fe}_x\text{NbSe}_2$  and  $\text{NbSe}_{2-x}\text{S}_x$ , illustrates its unusual character.

## EXPERIMENTAL SECTION

Polycrystalline samples of  $\text{Cu}_x\text{NbSe}_2$  were synthesized in two steps by solid state reaction. First, the mixtures of high-purity, cleaned fine powders of Cu (99.9%), Nb (99.9%), and Se (99.999%) in the appropriate stoichiometric ratios were heated in sealed evacuated silica glass tubes at a rate of 1 °C/min to 700 °C and held there for 120 h. Subsequently, the as-prepared powders were reground, repelletized, and sintered again, by being heated at a rate of 3 °C/min to 700 °C and held there for 48 h. The  $\text{NbSe}_{2-x}\text{S}_x$  samples were prepared in the same way. The identity and phase purity of the samples were determined by powder X-ray diffraction (PXRD) using a Bruker D8 Advance ECO instrument with Cu  $K\alpha$  radiation and a LYNXEYE-XE detector. To determine the unit cell parameters, profile fits were performed on the powder diffraction data through the use of the

FULLPROF diffraction suite using Thompson-Cox-Hastings pseudo-Voigt peak shapes.<sup>31</sup>

Measurements of the temperature-dependent electrical resistivity (four-contact method), specific heat, and magnetic susceptibility of the materials were performed in a DynaCool Quantum Design Physical Property Measurement System (PPMS). There was no indication of air sensitivity of the materials during the study.  $T_c$  values determined from susceptibility data were estimated conservatively.  $T_c$  was taken as the intersection of the extrapolations of the steepest slope of the susceptibility in the superconducting transition region and the normal state susceptibility; for resistivities, the midpoint of the resistivity  $\rho(T)$  transitions was taken, and for the specific heat data, the critical temperatures obtained from the equal area construction method were employed.

The temperature-dependent electron diffraction experiments were performed on a JEOL 2100F transmission electron microscope equipped with a Gatan liquid helium sample stage. Coherent electron diffraction patterns were recorded with a CCD camera and obtained from the same area in a single-crystal domain for each sample throughout the thermal process. For each sample, electron diffraction patterns acquired from several single-crystal domains were all consistent, with typical results shown here.

## RESULTS AND DISCUSSION

Panels B and C of Figure 1 show the powder X-ray diffraction patterns and unit cell parameters for  $\text{Cu}_x\text{NbSe}_2$  ( $0 \leq x \leq 0.09$ ), respectively. The results show that a single phase solid solution is indeed formed. The solubility limit for intercalated Cu in 2H-NbSe<sub>2</sub> is  $x = 0.09$ . At higher Cu contents, the cubic  $\text{Cu}_3\text{NbSe}_4$  phase is found as an impurity. Within the solid solution, unit cell parameters  $a$  and  $c$  both increase linearly with an increase in Cu content, in a Vegard's law type behavior:  $a$  increases linearly from 3.4432(4) Å ( $x = 0$ ) to 3.4507(1) Å ( $x = 0.09$ ), and  $c$  increases linearly from 12.5409(5) Å ( $x = 0$ ) to 12.6277(4) Å ( $x = 0.09$ ). The increase in  $c$  with an increase in Cu content is a signature that is characteristic of 3d metal intercalation in TMDCs.<sup>32</sup> The detailed changes in the crystallographic cell in

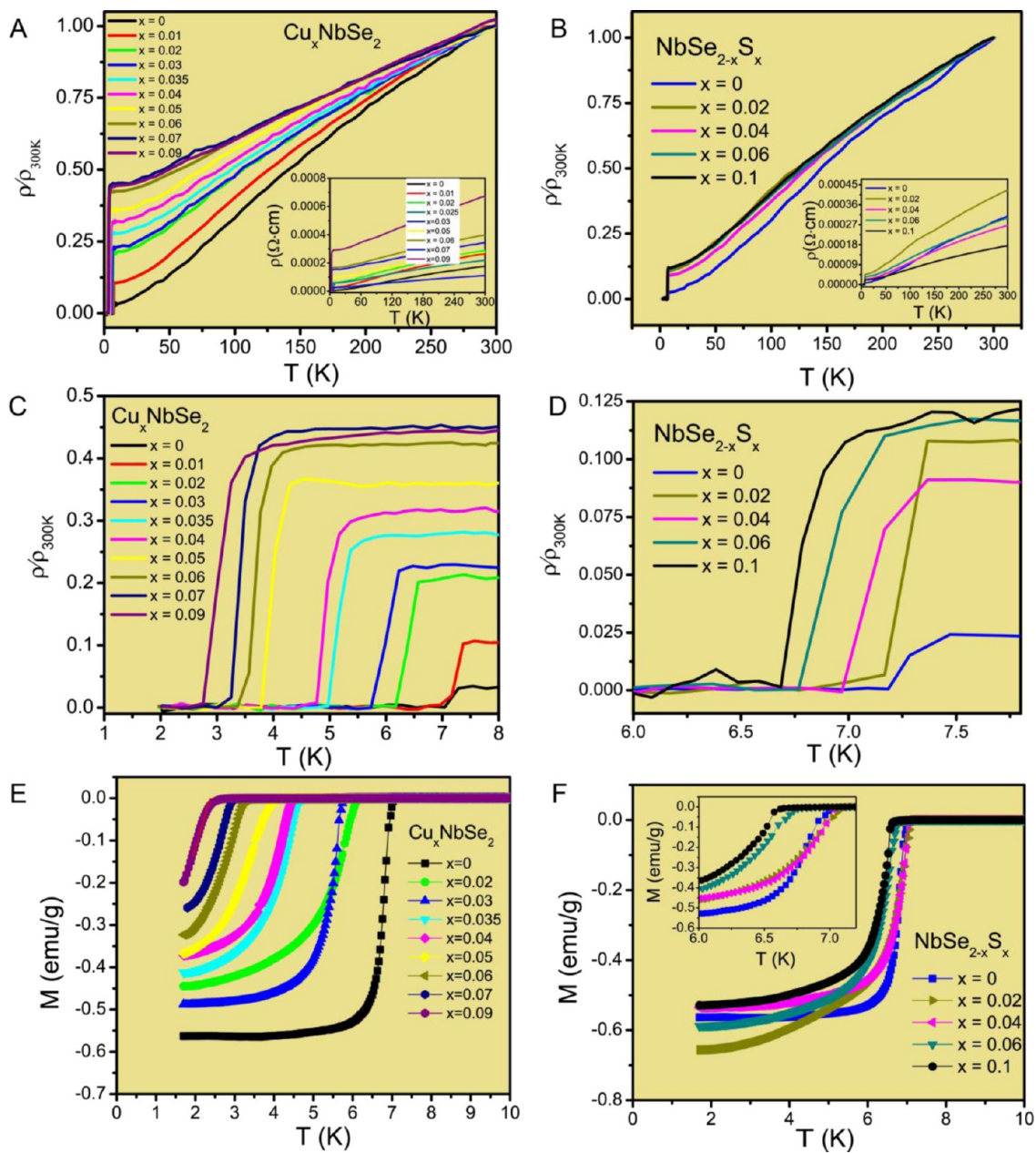


**Figure 2.** Transport characterization of the normal states and superconducting transitions for (A)  $\text{Cu}_x\text{NbSe}_2$  and (B)  $\text{NbSe}_{2-x}\text{S}_x$ . Temperature dependence of the resistivity ratio ( $\rho/\rho_{300\text{K}}$ ) for polycrystalline  $\text{Cu}_x\text{NbSe}_2$  ( $0 \leq x \leq 0.09$ ) and  $\text{NbSe}_{2-x}\text{S}_x$  ( $0 \leq x \leq 0.1$ ). (C and D) Enlarged temperature region showing the superconducting transitions. (E and F) Magnetic susceptibilities of  $\text{Cu}_x\text{NbSe}_2$  ( $0 \leq x \leq 0.09$ ) and  $\text{NbSe}_{2-x}\text{S}_x$  ( $0 \leq x \leq 0.1$ ) at the superconducting transitions. Applied DC fields are 20 Oe.

the  $\text{NbSe}_{2-x}\text{S}_x$  system are not the subject of this study and are not presented.

We next consider the temperature dependence of the normalized ( $\rho/\rho_{300\text{K}}$ ) resistivities of both  $\text{Cu}_x\text{NbSe}_2$  and  $\text{NbSe}_{2-x}\text{S}_x$ . Although careful interpretation of resistivities necessitates the use of data obtained on single crystals, consideration of the data on polycrystalline samples can provide some basic insights. Panels A and B of Figure 2 thus show the temperature dependence of the normalized electrical resistivities ( $\rho/\rho_{300\text{K}}$ ) for polycrystalline samples of  $\text{Cu}_x\text{NbSe}_2$  and  $\text{NbSe}_{2-x}\text{S}_x$ , respectively. The samples in both cases show a metallic temperature dependence ( $d\rho/dT > 0$ ) in the temperature region of 8–300 K. However, the relative resistances of the  $\text{Cu}_x\text{NbSe}_2$  samples decrease substantially less with temperature than those of  $\text{NbSe}_{2-x}\text{S}_x$ ; the residual

resistivity ratios [(resistivity at 300 K)/(resistivity just above  $T_c$ )] for the polycrystalline samples are, for example,  $\sim 29$  for  $\text{NbSe}_2$ ,  $\sim 9$  for  $\text{NbSe}_{1.9}\text{S}_{0.1}$ , and  $\sim 2$  for  $\text{Cu}_{0.09}\text{NbSe}_2$ . The factor of 15 difference between  $\text{NbSe}_2$  and  $\text{Cu}_{0.09}\text{NbSe}_2$  suggests that Cu may be an electronically disruptive dopant in  $\text{NbSe}_2$ . At low temperatures (see Figure 2C,D), a clear, sharp drop in  $\rho(T)$  is observed in all the  $\text{Cu}_x\text{NbSe}_2$  and  $\text{NbSe}_{2-x}\text{S}_x$  samples, signifying the onset of superconductivity at low temperatures.  $T_c$  decreases with a higher doping content in both cases. This trend is also clearly seen in the susceptibility data (Figure 2E,F); the onset of the negative magnetic susceptibility signaling the superconducting state shifts systematically to lower temperatures with an increase in  $x$  for both  $\text{Cu}_x\text{NbSe}_2$  and  $\text{NbSe}_{2-x}\text{S}_x$ .

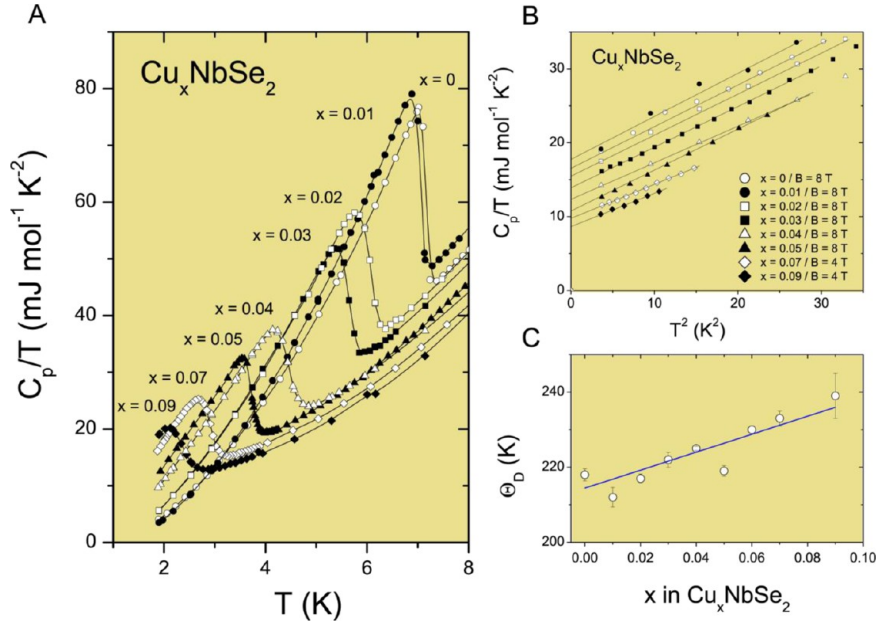


**Figure 3.** Heat capacity characterization of  $\text{Cu}_x\text{NbSe}_2$ . (A) Heat capacities through the superconducting transitions without an applied magnetic field for different compositions in  $\text{Cu}_x\text{NbSe}_2$ . (B) Heat capacities for  $\text{Cu}_x\text{NbSe}_2$  for different values of  $x$  at an applied magnetic field sufficiently high to fully suppress the superconductivity. Data were used to determine the electronic contribution to the specific heat and the Debye temperatures. (C) Debye temperature of  $\text{Cu}_x\text{NbSe}_2$  for different values of  $x$  obtained from fits to data in panel B.

**Table 1. Characterization of the Superconductivity in the  $\text{Cu}_x\text{NbSe}_2$  Family**

$x$ in $\text{Cu}_x\text{NbSe}_2$	0	0.01	0.02	0.03	0.035	0.04	0.05	0.06	0.07	0.09
$T_c$ (K)	7.16	7.05	6.04	5.6	5.2	4.46	3.8	3.18	2.9	2.3
$\gamma$ ( $\text{mJ mol}^{-1} \text{K}^{-2}$ )	17.4(20)	17.37(30)	15.58(17)	14.1(1)	–	12.11(10)	10.5(1)	10.4(1)	9.7(1)	8.8(1)
$\beta$ ( $\text{mJ mol}^{-1} \text{K}^{-4}$ )	0.56	0.61	0.56	0.53	–	0.52	0.56	0.49	0.47	0.44
$\Theta_D$ (K)	218(16)	212(26)	217(12)	222(20)	–	225(06)	219(14)	230(10)	233(20)	239(60)
$\Delta C/\gamma T_c$	2.04	2.15	1.94	1.96	–	1.81	1.79	1.57	1.68	1.62
$\lambda_{ep}$	0.81	0.82	0.76	0.73	–	0.67	0.65	0.60	0.59	0.55
$N(E_F)$ [states $\text{eV}^{-1}$ (formula unit) $^{-1}$ ]	4.08	4.17	3.76	3.45	–	3.07	2.71	2.82	2.60	2.39
$-dH_{c2}/dT$ (T/K)	1.95(4)	2.39(4)	2.29(4)	2.15(15)	2.01(3)	2.25(2)	1.45(4)	–	1.59(5)	–
$\mu_0 H_{c2}$ (T)	9.7(2)	11.7(2)	9.6(2)	8.3(6)	7.2(1)	7.0(1)	3.8(1)	–	3.2(1)	–
$\mu_0 H^p$ (T)	13.2	13.0	11.2	10.4	9.6	8.3	7.0	–	5.4	–
$\xi_{GL}(0)$ (nm)	5.8	5.3	5.9	6.3	6.7	6.9	9.3	–	10.1	–
$\mu_0 H_{c1}$ (T)	0.0158	0.0111	0.0100	0.0080	0.0065	–	0.0056	–	–	–
$\lambda_{GL}(0)$ (nm)	191	237	248	280	314	–	323	–	–	–
$\kappa_{GL}$	33	44	42	45	47	–	35	–	–	–
$\mu_0 H_c$ (mT)	209	185	160	133	111	–	78	–	–	–

More detailed information about the electronic properties and superconductivity of the  $\text{Cu}_x\text{NbSe}_2$  solid solution was obtained from specific heat measurements. Figure 3A shows the temperature dependence of the zero-field specific heat,  $C_p/T$  versus  $T$ , for selected  $\text{Cu}_x\text{NbSe}_2$  samples. The figure shows that all the materials display a large specific heat jump at  $T_c$ , an indication of bulk superconductivity. The superconducting transition temperatures are in excellent agreement with the  $T_c$  values determined from the  $\rho(T)$  and  $\chi(T)$  measurements. The normal state specific heats at low temperatures in the presence of a magnetic field large enough to suppress the superconductivity obey the relation  $C_p = \gamma T + \beta T^3$ , where  $\gamma$  and  $\beta$  describe the electronic and phonon contributions to the heat capacity, respectively. By fitting the data obtained in the 4 and 8 T applied fields (Figure 3B), we obtain the electronic specific heat coefficients ( $\gamma$ ) and phonon specific heat coefficients ( $\beta$ ). The normalized specific heat jump values ( $\Delta C/\gamma T_c$ ) thus

obtained from the data in panels A and B of Figure 3 range from 2.04 for  $2\text{H-NbSe}_2$  to 1.68 for  $\text{Cu}_{0.07}\text{NbSe}_2$ . These are all higher than the Bardeen–Cooper–Schrieffer (BCS) weak-coupling limit value (1.43) and clearly decrease with an increase in  $x$ . Using the fitted values of  $\beta$ , we estimate the Debye temperatures by the relation  $\theta_D = (12\pi \times 4nR/5\beta)^{1/3}$ , where  $n$  is the number of atoms per formula unit and  $R$  is the gas constant. The results (Figure 3C) show that the Debye temperatures increase modestly with increasing Cu content in  $\text{Cu}_x\text{NbSe}_2$  as the lattice becomes stiffer when some of the Se–Se VdW bonds are replaced by Se–Cu–Se bonds. These data are summarized in Table 1.

The dependence on  $x$  of the superconducting transition temperature and important electronic parameters for  $\text{Cu}_x\text{NbSe}_2$  determined from the specific heat data are summarized in Figure 4. Using the Debye temperature ( $\theta_D$ ) and the critical temperature ( $T_c$ ) and assuming that the electron–phonon

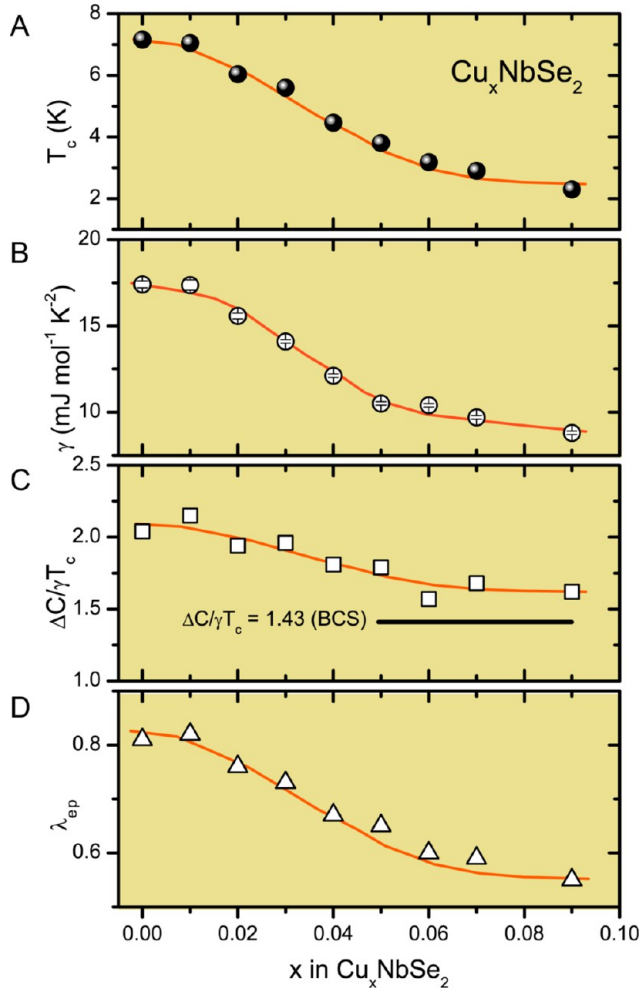


**Figure 4.** Superconducting transition temperatures for  $\text{Cu}_x\text{NbSe}_2$  and the associated electronic characteristics. (A) Superconducting transition temperature ( $T_c$ ) vs  $x$ . (B) Electronic contribution to the specific heat,  $\gamma$ , vs  $x$ . (C)  $\Delta C/\gamma T_c$  vs  $x$ . (D) Electron–phonon coupling constant,  $\lambda$ , vs  $x$  in  $\text{Cu}_x\text{NbSe}_2$ . An S-like character is observed for all parameters.

coupling constant ( $\lambda_{\text{ep}}$ ) can be calculated from the inverted McMillan formula:<sup>33</sup>

$$\lambda_{\text{ep}} = \frac{1.04 + \mu^* \ln\left(\frac{\theta_D}{1.45T_c}\right)}{(1 - 0.62\mu^*) \ln\left(\frac{\theta_D}{1.45T_c}\right) - 1.04}$$

The values of  $\lambda_{\text{ep}}$  obtained range from 0.81 for 2H-NbSe<sub>2</sub> to 0.55 for  $\text{Cu}_{0.09}\text{NbSe}_2$  (Table 1). These values suggest strong coupling superconductivity. With the Sommerfeld parameter ( $\gamma$ ) and the electron–phonon coupling ( $\lambda_{\text{ep}}$ ), the electron density of states at the Fermi level [ $N(E_F)$ ] can be calculated from the equation  $N(E_F) = \{3/[\pi^2 k_B^2 (1 + \lambda_{\text{ep}})]\} \gamma$ . This yields  $N(E_F)$  values that range from 4.08 states  $\text{eV}^{-1}$  (formula unit)<sup>-1</sup> for NbSe<sub>2</sub> to 2.39 states  $\text{eV}^{-1}$  (formula unit)<sup>-1</sup> for  $\text{Cu}_{0.09}\text{NbSe}_2$  (Table 1). The density of electronic states at the Fermi energy therefore clearly decreases when more Cu intercalates into 2H-NbSe<sub>2</sub>. It can be seen in Figure 4 that the electronic parameters derived from the specific heat for  $\text{Cu}_x\text{NbSe}_2$  show an S-shaped character that corresponds to that for the superconducting transition temperatures.

The superconducting transitions for selected  $\text{Cu}_x\text{NbSe}_2$  samples were further examined through temperature-dependent measurements of the electrical resistivity and magnetization under an applied magnetic field, with the goal of determining the critical fields at 0 K,  $\mu_0 H_{c1}(0)$ ,  $\mu_0 H_{c2}(0)$ , and  $\mu_0 H_c(0)$ . First, we consider the resistivity measurements employed to determine  $\mu_0 H_{c2}(0)$ . The  $\rho(T, H)$  data obtained for  $\text{Cu}_x\text{NbSe}_2$  ( $x = 0$  or 0.05) are shown as an example in panels A and B of Figure 5. On the basis of the  $T_c$  determined resistively under different magnetic fields, the upper critical field values,  $\mu_0 H_{c2}$ , are plotted versus temperature in Figure 5C. A clear linear dependence of  $\mu_0 H_{c2}$  versus  $T$  is seen near  $T_c$  for all samples: the solid lines through the data show the best linear fits. The initial slopes ( $dH_{c2}/dT$ ) for  $\text{Cu}_x\text{NbSe}_2$  are listed in Table 1. From these data, we estimate the zero-temperature upper critical fields (top inset in Figure 5F) to range from 9.96 T for NbSe<sub>2</sub> to 3.72 T for  $\text{Cu}_{0.07}\text{NbSe}_2$ , using the Werthamer–Helfand–Hohenberg (WHH) expression for the dirty limit superconductivity,  $\mu_0 H_{c2} = -0.693 T_c (dH_{c2}/dT_c)$ .<sup>33–37</sup> The results are summarized in Table 1; the  $\mu_0 H_{c2}$  for  $x = 0.01$  is larger than that for  $x = 0$ , likely because of vortex pinning, and it then decreases with an increase in  $x$ . The Pauli limiting field for  $\text{Cu}_x\text{NbSe}_2$  was estimated from  $\mu_0 H^P = 1.86 T_c$ . The obtained values of  $\mu_0 H^P$  are only slightly larger than the estimated  $\mu_0 H_{c2}$ . Finally, using the equation  $\mu_0 H_{c2} = \phi_0 / (2\pi \xi_{\text{GL}}^2)$ , where  $\phi_0$  is the quantum of flux, the Ginzburg–Landau coherence length [ $\xi_{\text{GL}}(0)$ ] can be estimated to range from  $\sim 5.3$  nm for  $\text{Cu}_{0.01}\text{NbSe}_2$  to  $\sim 10.1$  nm for  $\text{Cu}_{0.07}\text{NbSe}_2$  (Table 1).

To determine  $\mu_0 H_{c1}(0)$ , the superconducting transition for selected  $\text{Cu}_x\text{NbSe}_2$  samples was further examined through temperature-dependent measurements of the magnetization under increasing applied magnetic field  $M(H)$ . The main panel of Figure 5D shows the data for  $\text{Cu}_{0.05}\text{NbSe}_2$ , and how  $\mu_0 H_{c1}$  was determined, as an example. First, to estimate the demagnetization factor ( $N$ ), low-field magnetization measurements as a function of field  $M(H)$  were performed at 1.7, 2, 2.5, 3, and 3.5 K, as shown in the main panel of Figure 5D. At low magnetic fields, the experimental data can be fit with the linear formula  $M_{\text{fit}} = a + bH$ . Assuming that the initial linear response to a magnetic field is perfectly diamagnetic ( $dM/dH = -1/4\pi$ ) for these bulk superconductors, we obtained values of  $N$ , the demagnetization factor, of 0.1–0.7 [from  $-4\pi\chi_V = 1/(1 - N)$ , where  $\chi_V = dM/dH$  is actually a fitted slope from the main panel of Figure 5D] that are consistent with the sample shape. The  $M(H) - M_{\text{fit}}$  data are plotted versus the applied magnetic field ( $H$ ) in the inset of Figure 5D.  $\mu_0 H_{c1}^*$  is taken as the field where  $M$  deviates by  $\sim 2\%$  above the fitted line ( $M_{\text{fit}}$ ), as is the common practice.<sup>38</sup> Taking into account the demagnetization factor ( $N$ ), we can calculate the lower critical field at temperature  $T$ ,  $\mu_0 H_{c1}(T)$ , from the formula  $\mu_0 H_{c1}(T) = \mu_0 H_{c1}^*(T)/(1 - N)$ .<sup>39,40</sup> Figure 5E presents  $\mu_0 H_{c1}$  as a function of temperature for selected  $\text{Cu}_x\text{NbSe}_2$  samples. The estimation of  $\mu_0 H_{c1}(0)$  is then possible by fitting the  $\mu_0 H_{c1}(T)$  data to the formula  $\mu_0 H_{c1}(T) = \mu_0 H_{c1}(0)[1 - (T/T_c)^2]$ , which is represented by the solid lines. The estimated zero-temperature lower critical fields  $\mu_0 H_{c1}(0)$  (see the bottom of the inset of Figure 5F) for  $\text{Cu}_x\text{NbSe}_2$  ( $x = 0, 0.01, 0.02, 0.03, 0.035, \text{ and } 0.05$ ) range from 0.0158 T for NbSe<sub>2</sub> to 0.0056 T for  $\text{Cu}_{0.05}\text{NbSe}_2$ . From the relation  $\mu_0 H_{c1}(0) = (\phi_0/4\pi\lambda^2) \ln(\lambda_{\text{GL}}/\xi_{\text{GL}})$ , we numerically find another important superconducting parameter, the magnetic penetration depth ( $\lambda_{\text{GL}}$ ). This parameter ranges from 191 nm for NbSe<sub>2</sub> to 323 nm for  $\text{Cu}_{0.05}\text{NbSe}_2$ . The Ginzburg–Landau parameter  $\kappa_{\text{GL}} = \lambda_{\text{GL}}/\xi_{\text{GL}}$

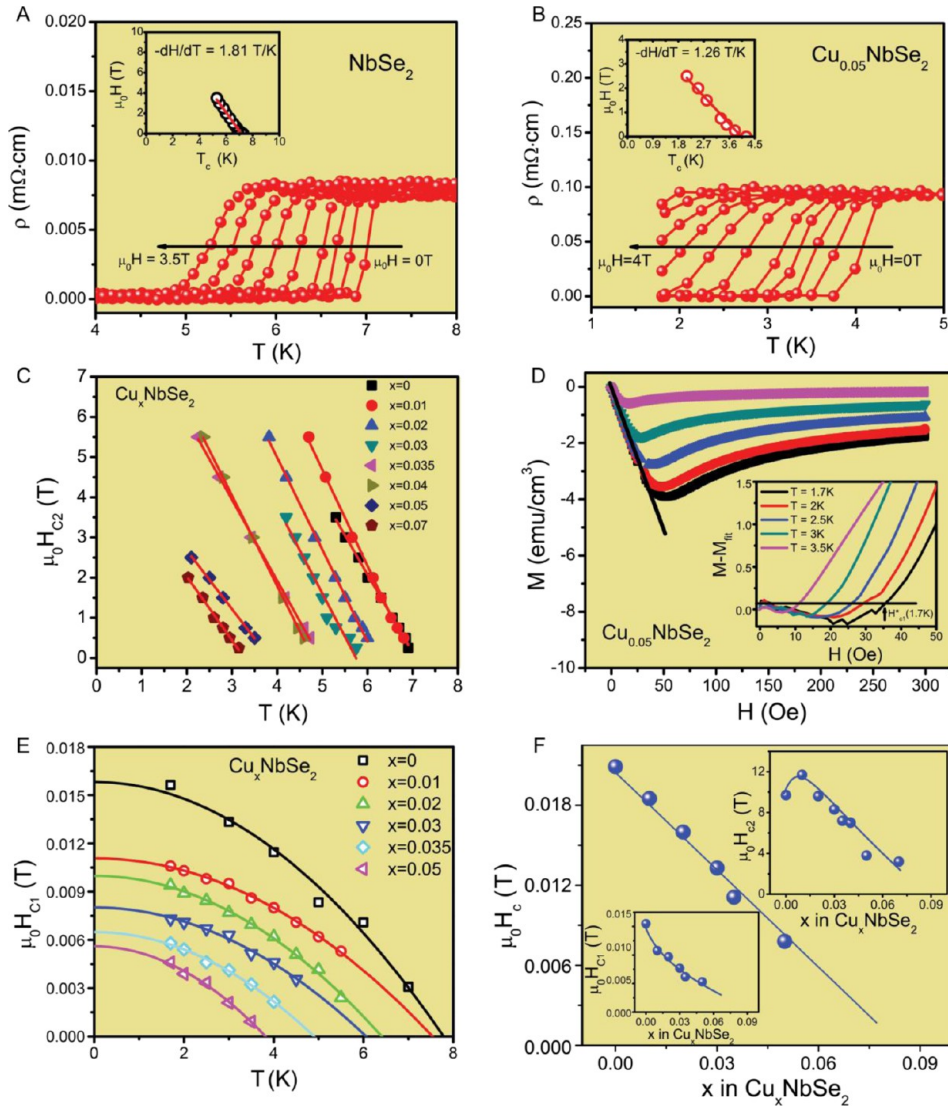


**Figure 5.** Characterization of the critical fields of  $\text{Cu}_x\text{NbSe}_2$ . (A and B) Low-temperature resistivity at various applied fields for the examples of  $\text{NbSe}_2$  and  $\text{Cu}_{0.05}\text{NbSe}_2$ . (C) Temperature dependence of the upper critical field ( $\mu_0H_{c2}$ ) for  $\text{Cu}_x\text{NbSe}_2$ . (D) Magnetic susceptibility at low applied magnetic fields at various applied temperatures for  $\text{Cu}_{0.05}\text{NbSe}_2$ . The inset shows  $M - M_{\text{fit}}$  vs  $H$ . (E) Temperature dependence of the lower critical field ( $\mu_0H_{c1}$ ) for  $\text{Cu}_x\text{NbSe}_2$ . (F) Thermodynamic critical field vs  $x$ .

is then calculated and confirms type II superconductivity in  $\text{Cu}_x\text{NbSe}_2$ . The thermodynamic critical field  $\mu_0H_c = (\mu_0H_{c1} \times \mu_0H_{c2}/\ln \kappa)^{0.5}$  is shown in Figure 5F.  $\mu_0H_c$  decreases linearly with increasing Cu content in  $\text{Cu}_x\text{NbSe}_2$ . These parameters are summarized in Table 1.

Figure 6 shows a comparison of the electron diffraction patterns in the basal plane  $hk0$  reciprocal lattice for  $\text{NbSe}_2$  and  $\text{Cu}_{0.06}\text{NbSe}_2$ , both at room temperature and at 10 K. The hexagonal symmetry is clearly seen in the intense diffraction spots that arise from the basic structure for both materials at both temperatures. At 10 K, the sharp superlattice diffraction spots because of the CDW (between the intense spots from the basic lattice) are clearly seen for pure  $\text{NbSe}_2$ . Their measured nearly commensurate  $q$  vector is  $0.337a^*$ , and they appeared sharply on cooling between 30 and 40 K, consistent with previous observations for  $2\text{H-NbSe}_2$ .<sup>41,42</sup> The measured widths of the superlattice spots suggest an in-plane coherence of 15–20 nm. Similar, but significantly different in detail, diffraction evidence of CDW formation is also clearly seen in  $\text{Cu}_{0.06}\text{NbSe}_2$ . In this case, the spots are less sharp, an indication of a decrease

in coherent diffracting volume, with a measured in-plane coherence of  $\leq 10$  nm. The  $q$  vector of the CDW has changed somewhat, to  $0.370a^*$  for  $\text{Cu}_{0.06}\text{NbSe}_2$ . Finally, diffuse electron scattering characteristic of CDW formation with short coherence lengths was not clearly visible in undoped  $\text{NbSe}_2$  above its three-dimensional (3D) CDW transition; i.e., the onset of the 3D CDW was sharp in temperature. In contrast, however, diffuse scattering persists up to room temperature in  $\text{Cu}_{0.06}\text{NbSe}_2$ , indicative of short coherence length CDW fluctuations in the Cu-intercalated material up to quite high temperatures. For  $\text{Cu}_{0.06}\text{NbSe}_2$ , no sharp transition to 3D ordering is observed; rather, the  $q = 0.37a^*$  diffraction spots visible at 10 K appear to grow approximately continuously out of the diffuse scattering upon cooling. It is natural to ask whether the Cu intercalation disrupts the CDW coherence more in plane than out of plane. This question can be addressed by looking at a larger volume of the reciprocal lattice, shown in Figure 7. Far from the origin of the reciprocal lattice, the curvature of the Ewald sphere allows higher index zones (e.g.,  $hk1$ ,  $hk2$ , etc.) to be sampled. The results for these types

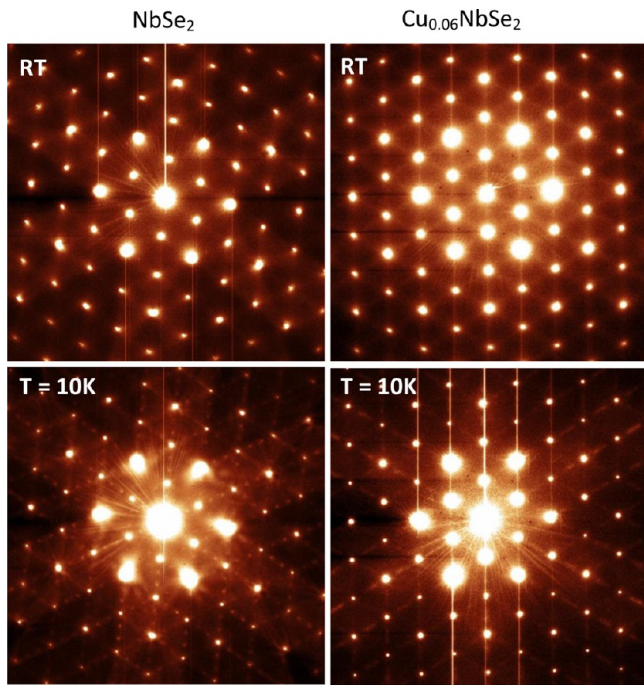


**Figure 6.** Temperature-dependent electron diffraction characterization of the CDWs in  $\text{NbSe}_2$  and  $\text{Cu}_{0.06}\text{NbSe}_2$ . Typical electron diffraction patterns (along the  $[001]$  zone axis, i.e., in the  $hk0$  reciprocal lattice plane) obtained from pure  $\text{NbSe}_2$  (left) and  $\text{Cu}_{0.06}\text{NbSe}_2$  (right). The hexagonal symmetry is clearly seen. For both samples, patterns at room temperature (RT) and low temperatures were obtained from the same area. The vertical streaks are artifacts from the CCD camera. Kikuchi bands are seen in some of the patterns. The CDW in both cases is evidenced by lines of weaker diffraction spots between the main structure spots in the data at 10 K. For the  $\text{Cu}_{0.06}\text{NbSe}_2$  material, diffuse streaks in the diffraction pattern along these lines persist to room temperature.

of reciprocal space probes are shown for diffraction from 2H- $\text{NbSe}_2$  and  $\text{Cu}_{0.06}\text{NbSe}_2$  in Figure 7. Again the hexagonal symmetry of the basic structure is clearly seen, as are the superlattice spots due to CDW formation. (The bright rings of spots distant from the origin arise from the intersection of the Ewald sphere with the higher-order basic structure reciprocal lattice planes.) The degradation of the intensity of the superlattice spots on going to higher zones is much larger in the case of pure  $\text{NbSe}_2$  than it is for  $\text{Cu}_{0.06}\text{NbSe}_2$ , and therefore, these diffraction patterns show that the disruption of the CDW is more pronounced perpendicular to the planes than in plane, i.e., that the 3D CDW coherence is more disrupted than the in-plane coherence by Cu intercalation. In both cases, the CDW spots are strong in the  $hk0$  zone (near the origin of the reciprocal lattice), consistent with previous studies indicating that the CDW is still present in single-layer  $\text{NbSe}_2$ .<sup>43</sup>

Finally, the superconductivity phase diagram as a function of doping level for 2H- $\text{Cu}_x\text{NbSe}_2$  is summarized in Figure 8. For comparison, the superconductivity phase diagram for  $\text{NbSe}_{2-x}\text{S}_x$  ( $0 \leq x \leq 0.1$ ) from the study presented here is included, as is the same information for  $\text{Fe}_x\text{NbSe}_2$  taken from ref 44. The  $T_c$  values extracted from the three kinds of measurements performed here for  $\text{Cu}_x\text{NbSe}_2$  (resistivity, magnetic susceptibility, and heat capacity) are all consistent; the  $x$  dependence of  $T_c$  displays an S-like shape in the  $\text{Cu}_x\text{NbSe}_2$  system, but not in the other systems. The  $T_c$  of pure 2H- $\text{NbSe}_2$  is 6.5 K,<sup>45</sup> and therefore, the very small change in  $T_c$

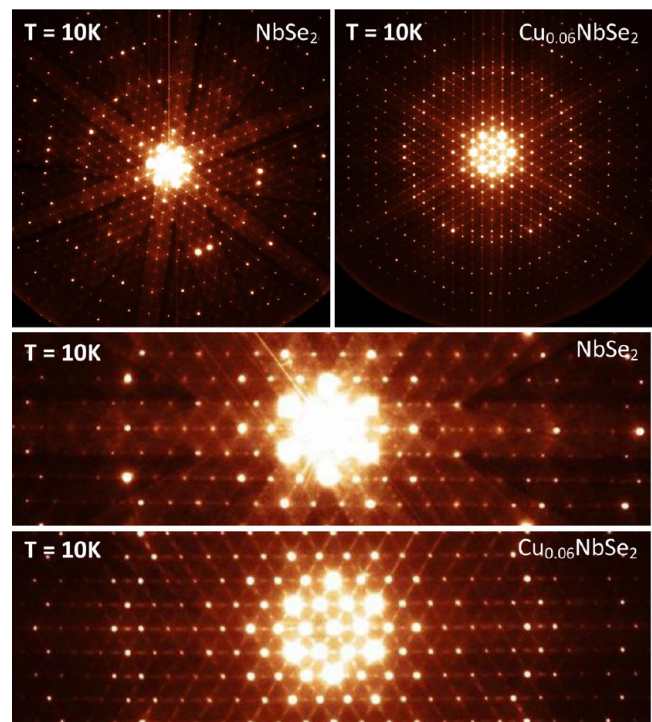


**Figure 7.** Electron diffraction patterns at 10 K over a wider volume of reciprocal space in  $\text{NbSe}_2$  and  $\text{Cu}_{0.06}\text{NbSe}_2$ . The intensity distributions of the CDW reflections strongly suggest the following. (1) The atomic displacements associated with the CDW modulation are longitudinal in both cases, and (2) the CDW modulation is relatively weakly correlated between layers (along the  $c$ -axis) for both materials. For  $\text{Cu}_{0.06}\text{NbSe}_2$ , the correlation of the CDW along the  $c$ -axis is weaker, based on the fact that the intensities of the CDW diffuse reflections remain strong close to the  $hk1$  Laue zone. Kikuchi bands and the hexagonal symmetry of the patterns are clearly seen.

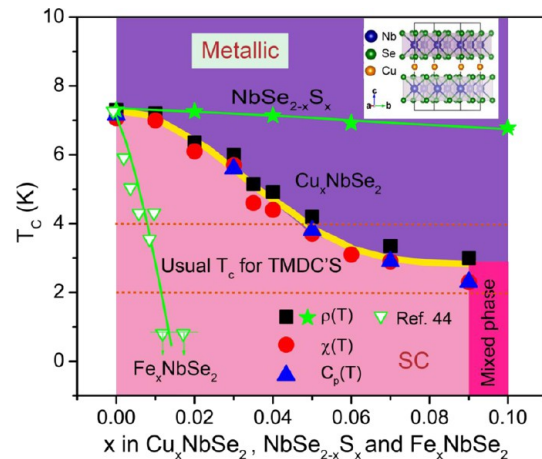


**Figure 8.** Superconducting phase diagram for 2H- $\text{Cu}_x\text{NbSe}_2$  compared to those of 2H- $\text{NbSe}_{2-x}\text{S}_x$  from the study presented here and 2H- $\text{Fe}_x\text{NbSe}_2$  from ref 44. The usual range of  $T_c$  values for transition metal dichalcogenides is illustrated by the dashed lines. “SC” and “metallic” label the superconducting and metallic regions for  $\text{Cu}_x\text{NbSe}_2$ , respectively. The labels  $\rho(T)$ ,  $\chi(T)$ , and  $C_p(T)$  are the  $T_c$  values determined for the materials in this study from resistivity, magnetic susceptibility, and specific heat characterization, respectively. The limit of the  $\text{Cu}_x\text{NbSe}_2$  solubility is  $x = 0.09$ ; beyond that  $x$  value, the materials contain multiple phases (the solubility extends to at least  $x = 0.1$  for  $\text{NbSe}_{2-x}\text{S}_x$ ). The top right inset shows a schematic of the crystal structure of  $\text{Cu}_x\text{NbSe}_2$ .

of the sulfur-doped material may not be surprising. (Work on  $\text{Cu}_x\text{NbS}_2$  similar to that performed in the study presented here may therefore be of interest in the future.) In contrast, intercalated Fe may be considered as a magnetic ion, with the magnetism leading to a very rapid suppression of  $T_c$  with an increasing Fe content. Therefore, nonmagnetic chemically different Cu intercalation is naively expected to act somewhere between the Fe- and S-doped extremes, although not with an S-shaped behavior; there are no previously known examples of an S-shaped suppression of  $T_c$  by substitution or doping in a single-phase material.

## CONCLUSION

$\text{Cu}_x\text{NbSe}_2$  ( $0 \leq x \leq 0.09$ ) was prepared by a solid state method. The electronic properties, including resistivity, heat capacity, and critical fields, were studied in detail and indicate that copper doping suppresses the superconductivity in  $\text{NbSe}_2$  in an unexpected way; the electronic properties and  $x$ -dependent electronic phase diagram show that the superconducting transition temperature of Cu-intercalated  $\text{NbSe}_2$  shows an unusual S-shaped behavior. The underlying reason for this usual S-shape behavior of  $T_c$  and the electronic characteristics that give rise to it have not been determined here. However, on the basis of the fact that the  $T_c$  is unusually high for pure  $\text{NbSe}_2$  and then settles to the usual value for TMDCs for  $\text{Cu}_x\text{NbSe}_2$ , it is not unreasonable to speculate that Cu doping destroys the higher-energy pairing channel that makes  $\text{NbSe}_2$  unusual among the layered TMDCs. We speculate that this may be due to either the electron doping of the  $\text{NbSe}_2$  layer that results in Cu intercalation or the nonmagnetic disorder introduced by the Cu intercalation. The lower  $T_c$  cannot, for example, simply be due to a strengthening of the competing CDW state for a non-zero  $x$  in  $\text{Cu}_x\text{NbSe}_2$ , because the electron diffraction studies show that such strengthening is clearly not the case. It may, however, be that the Cu intercalation both disrupts the coherence of the CDW and simultaneously suppresses the pairing channel that gives rise to the higher  $T_c$  in  $\text{NbSe}_2$ . Future detailed characterization experiments and theoretical treatments will be required to determine whether this speculation is indeed the case.

## ACKNOWLEDGMENTS

The research at Princeton University on sample synthesis and structural, resistive, and susceptibility characterization was supported by the U.S. Department of Energy office of Basic Energy Sciences (DOE BES) through Grant DE-FG02-98ER45706. All work in Gdansk, Poland, including specific heat measurements and their interpretation, was supported by the National Science Centre (Poland), through Grant UMO-2015/19/B/ST3/03127. The electron diffraction study at Brookhaven National Laboratory was supported by the DOE BES, by the Materials Sciences and Engineering Division under Contract DE-SC0012704, and through the use of the Center

for Functional Nanomaterials. The authors thank F. von Rohr, L. MÜchler, and T. Kong for useful discussions.

## REFERENCES

- (1) Withers, R. L.; Bursill, L. A. The structure of the incommensurate superlattices of  $2\text{H-TaSe}_2$ . *Philos. Mag. B* **1981**, *43*, 635–672.
- (2) Arguello, C. J.; Chockalingam, S. P.; Rosenthal, E. P.; Zhao, L.; Gutiérrez, C.; Kang, J. H.; Chung, W. C.; Fernandes, R. M.; Jia, S.; Millis, A. J.; Cava, R. J.; Pasupathy, A. N. Visualizing the charge density wave transition in  $2\text{H-NbSe}_2$  in real space. *Phys. Rev. B: Condens. Matter Mater. Phys.* **2014**, *89*, 235115.
- (3) Soumyanarayanan, A.; Yee, M. M.; He, Y.; van Wezel, J.; Rahn, D. J.; Rossnagel, K.; Hudson, E. W.; Norman, M. R.; Hoffman, J. E. Quantum phase transition from triangular to stripe charge order in  $\text{NbSe}_2$ . *Proc. Natl. Acad. Sci. U. S. A.* **2013**, *110*, 1623–1627.
- (4) Matthias, B. T.; Geballe, T. H.; Compton, V. B. Superconductivity. *Rev. Mod. Phys.* **1963**, *35*, 1.
- (5) Revolinsky, E.; Lautenschlager, E. P.; Armitage, C. H. Layer structure superconductor. *Solid State Commun.* **1963**, *1*, 59–61.
- (6) Wilson, J. A.; Di Salvo, F. J.; Mahajan, S. Charge-density waves in metallic, layered, transition-metal dichalcogenides. *Phys. Rev. Lett.* **1974**, *32*, 882.
- (7) Boaknin, E.; Tanatar, M. A.; Paglione, J.; Hawthorn, D.; Ronning, F. R.; Hill, W.; Sutherland, M.; Taillefer, L.; Sonier, J.; Hayden, S. M.; Brill, J. W. Heat conduction in the vortex state of  $\text{NbSe}_2$ : evidence for multiband superconductivity. *Phys. Rev. Lett.* **2003**, *90*, 117003.
- (8) Suderow, H.; Tissen, V. G.; Brison, J. P.; Martínez, J. L.; Vieira, S. Pressure induced effects on the fermi surface of superconducting  $2\text{H-NbSe}_2$ . *Phys. Rev. Lett.* **2005**, *95*, 117006.
- (9) Du, C. H.; Lin, W. J.; Su, Y.; Tanner, B. K.; Hatton, P. D.; Casa, D.; Keimer, B.; Hill, J. P.; Oglesby, C. S.; Hohl, H. X-ray scattering studies of  $2\text{H-NbSe}_2$ , a superconductor and charge density wave material, under high external magnetic fields. *J. Phys.: Condens. Matter* **2000**, *12*, 5361–5370.
- (10) Xi, X. X.; Zhao, L.; Wang, Z. F.; Berger, H.; Forró, L.; Shan, L. F. J.; Mak, K. F. Strongly enhanced charge-density-wave order in monolayer  $\text{NbSe}_2$ . *Nat. Nanotechnol.* **2015**, *10*, 765–770.
- (11) Ménard, G. C.; Guissart, S.; Brun, C.; Pons, S.; Stolyarov, V. S.; Debontridder, F.; Leclerc, M. V.; Janod, E.; Cario, L.; Roditchev, D.; Simon, P.; Cren, T. Coherent long-range magnetic bound states in a superconductor. *Nat. Phys.* **2015**, *11*, 1013–1016.
- (12) Kiss, T.; Yokoya, T.; Chainani, A.; Shin, S.; Hanaguri, T.; Nohara, M.; Takagi, H. Hidden Charge-Density-Wave Order in a Low- $T_c$  Superconductor  $2\text{H-NbSe}_2$ . <https://arxiv.org/vc/cond-mat/papers/0310/0310326v1.pdf>.
- (13) Johannes, M. D.; Mazin, I. I.; Howells, C. A. Fermi-surface nesting and the origin of the charge-density wave in  $\text{NbSe}_2$ . *Phys. Rev. B: Condens. Matter Mater. Phys.* **2006**, *73*, 205102.
- (14) Corcoran, R. C.; Meeson, P. J.; Onuki, Y.; Probst, P. A.; Springford, M.; Takita, K.; Harima, H.; Guo, G. Y.; Gyorffy, B. L. Quantum oscillations in the mixed state of the type II superconductor  $2\text{H-NbSe}_2$ . *J. Phys.: Condens. Matter* **1994**, *6*, 4479–4492.
- (15) Tsuei, C. C.; Kirtley, J. R. d-Wave pairing symmetry in cuprate superconductors—fundamental implications and potential applications. *Phys. C* **2002**, *367*, 1–8.
- (16) Souma, S.; Machida, Y.; Sato, T.; Takahashi, T.; Matsui, H.; Wang, S. C.; Ding, H.; Kaminski, A.; Campuzano, J. C.; Sasaki, S.; Kadowaki, K. The origin of multiple superconducting gaps in  $\text{MgB}_2$ . *Nature* **2003**, *423*, 65–67.
- (17) Örd, T.; Kristoffel, N. Modeling  $\text{MgB}_2$  two-gap superconductivity. *Phys. C* **2002**, *370*, 17–20.
- (18) Kristoffel, N.; Örd, T.; Rågo, K.  $\text{MgB}_2$  two-gap superconductivity with intra- and interband couplings. *EPL* **2003**, *61*, 109–115.
- (19) Huang, C. L.; Lin, J.-Y.; Chang, Y. T.; Sun, C. P.; Shen, H. Y.; Chou, C. C.; Berger, H.; Lee, T. K.; Yang, H. D. Experimental evidence for a two-gap structure of superconducting  $\text{NbSe}_2$ : A specific-heat study in external magnetic fields. *Phys. Rev. B: Condens. Matter Mater. Phys.* **2007**, *76*, 212504.





- (20) Boaknin, E.; Tanatar, M. A.; Paglione, J.; Hawthorn, D.; Ronning, F.; Hill, R. W.; Sutherland, M.; Taillefer, L.; Sonier, J.; Hayden, S. M.; Brill, J. W. Heat Conduction in the Vortex State of NbSe<sub>2</sub>: Evidence for Multiband Superconductivity. *Phys. Rev. Lett.* **2003**, *90*, 117003.
- (21) Zehetmayer, M.; Weber, H. W. Experimental evidence for a two-band superconducting state of NbSe<sub>2</sub> single crystals. *Phys. Rev. B: Condens. Matter Mater. Phys.* **2010**, *82*, 014524.
- (22) Fletcher, J. D.; Carrington, A.; Diener, P.; Rodière, P.; Brison, J. P.; Prozorov, R.; Olheiser, T.; Giannetta, R. W. Penetration Depth Study of Superconducting Gap Structure of 2H-NbSe<sub>2</sub>. *Phys. Rev. Lett.* **2007**, *98*, 057003.
- (23) Rodrigo, J. G.; Vieira, S. STM study of multiband superconductivity in NbSe<sub>2</sub> using a superconducting tip. *Phys. C* **2004**, *404*, 306–310.
- (24) Guillamon, I.; Suderow, H.; Guinea, F.; Vieira, S. Intrinsic atomic-scale modulations of the superconducting gap of 2H-NbSe<sub>2</sub>. *Phys. Rev. B: Condens. Matter Mater. Phys.* **2008**, *77*, 134505.
- (25) Noat, Y.; Cren, T.; Debontridder, F.; Roditchev, D.; Sacks, W.; Toulemonde, P.; San Miguel, A. Signatures of multigap superconductivity in tunneling spectroscopy. *Phys. Rev. B: Condens. Matter Mater. Phys.* **2010**, *82*, 014531.
- (26) Rahn, D. J.; Hellmann, S.; Kalläne, M.; Sohr, C.; Kim, T. K.; Kipp, L.; Rossnagel, K. Gaps and kinks in the electronic structure of the superconductor 2H-NbSe<sub>2</sub> from angle-resolved photoemission at 1 K. *Phys. Rev. B: Condens. Matter Mater. Phys.* **2012**, *85*, 224532.
- (27) Yokoya, T.; Kiss, T.; Chainani, A.; Shin, S.; Nohara, M.; Takagi, H. Fermi Surface Sheet-Dependent Superconductivity in 2H-NbSe<sub>2</sub>. *Science* **2001**, *294*, 2518–2520.
- (28) Tonjes, W. C.; Greanya, V. A.; Liu, R.; Olson, C. G.; Molinié, P. Charge-density-wave mechanism in the 2H-NbSe<sub>2</sub> family: Angle-resolved photoemission studies. *Phys. Rev. B: Condens. Matter Mater. Phys.* **2001**, *63*, 235101.
- (29) Xi, X. X.; Wang, Z. F.; Zhao, W. W.; Park, J. H.; Law, K. T.; Berger, H.; Forró, L. J.; Shan, J.; Mak, K. F. Ising pairing in superconducting NbSe<sub>2</sub> atomic layers. *Nat. Phys.* **2016**, *12*, 139–144.
- (30) Koh, Y. Y.; Kim, Y. K.; Jung, W. S.; Han, G. R.; Park, S. R.; Leem, C. S.; Kim, C.; Song, D. J.; Kyung, W. S.; Choi, H. Y.; Yang, L. X.; He, C.; Chen, F.; Feng, D. L.; Kim, C. Photoemission studies of Cu intercalated NbSe<sub>2</sub>. *J. Phys. Chem. Solids* **2011**, *72*, 565–567.
- (31) Rodríguez-Carvajal, J. Recent developments of the program FULLPROF. *Commission on Powder Diffraction* **2001**, *26*, 12–19.
- (32) Voorhoeve, J. M.; van den Berg, N.; Robbins, M. Intercalation of the Niobium-Diselenide Layer Structure by First-Row Transition Metals. *J. Solid State Chem.* **1970**, *1*, 134–137.
- (33) McMillan, W. L. Transition temperature of strong-coupled superconductors. *Phys. Rev.* **1968**, *167*, 331.
- (34) Wilson, J. A.; Barker, A. S.; Di Salvo, F. J.; Ditzemberger, J. A. Ditzemberger, Infrared properties of the semimetal TiSe<sub>2</sub>. *Phys. Rev. B: Condens. Matter Mater. Phys.* **1978**, *18*, 2866–2875.
- (35) Kohn, W. Excitonic Phases. *Phys. Rev. Lett.* **1967**, *19*, 439–442.
- (36) Werthamer, N. R.; Helfand, E.; Hohenberg, P. C. Temperature and Purity Dependence of the Superconducting Critical Field, H<sub>c2</sub>. III. Electron Spin and Spin-Orbit Effects. *Phys. Rev.* **1966**, *147*, 295.
- (37) Kresin, V. Z.; Wolf, S. A. *Fundamentals of superconductivity*; Plenum Press: New York, 1990; pp 150–153.
- (38) Luo, H. X.; Xie, W. W.; Tao, J.; Pletikoscic, I.; Valla, T. G.; Sahasrabudhe, S.; Osterhoudt, G.; Sutton, E.; Burch, K. S.; Seibel, E. M.; Krizan, J. W.; Zhu, Y. M.; Cava, R. J. Differences in chemical doping matter - Superconductivity in Ti<sub>1-x</sub>Ta<sub>x</sub>Se<sub>2</sub> but not in Ti<sub>1-x</sub>Nb<sub>x</sub>Se<sub>2</sub>. *Chem. Mater.* **2016**, *28*, 1927–1935.
- (39) Winiarski, M. J.; Wiendlocha, B.; Gołab, S.; Kushwaha, S. K.; Wiśniewski, P.; Kaczorowski, D.; Thompson, J. D.; Cava, R. J.; Klimczuk, T. Superconductivity in CaBi<sub>2</sub>. *Phys. Chem. Chem. Phys.* **2016**, *18*, 21737–21745.
- (40) Yadav, C. S.; Paulose, P. L. Upper critical field, lower critical field and critical current density of FeTe<sub>0.60</sub>Se<sub>0.40</sub> single crystal. *New J. Phys.* **2009**, *11*, 103046.
- (41) Kiss, T.; Yokoya, T.; Chainani, A.; Shin, S.; Hanaguri, T.; Nohara, M.; Takagi, H. Charge-order-maximized momentum dependent superconductivity. *Nat. Phys.* **2007**, *3*, 720–725.
- (42) Naik, I.; Rastogi, A. K. Charge density wave and superconductivity in 2H- and 4H-NbSe<sub>2</sub>: A revisit. *Pramana* **2011**, *76*, 957–963.
- (43) Ugeda, M. M.; Bradley, A. J.; Zhang, Y.; Onishi, S.; Chen, Y.; Ruan, W.; Ojeda-Aristizabal, C.; Ryu, H.; Edmonds, M. T.; Tsai, H. Z.; Riss, A.; Mo, S. K.; Lee, D. H.; Zettl, A.; Hussain, Z.; Shen, Z. X.; Crommie, M. F. Characterization of collective ground states in single-layer NbSe<sub>2</sub>. *Nat. Phys.* **2016**, *12*, 92–97.
- (44) Hauser, J. J.; Robbins, M.; DiSalvo, F. J. Effect of 3d Impurities on the Superconducting Transition Temperature of the Layered Compound NbSe<sub>2</sub>. *Phys. Rev. B* **1973**, *8*, 1038–1042.
- (45) Fisher, W. G.; Sienko, M. J. Stoichiometry, structure, and physical properties of niobium disulfide. *Inorg. Chem.* **1980**, *19*, 39–43.

